Role of the vertical pressure gradient in wave boundary layers

Jensen, Karsten Lindegård; Sumer, B. Mutlu; Vittori, Giovanna ; Blondeaux, Paolo

Published in:
Proceedings of the 34th International Conference on Coastal Engineering

Publication date:
2014

ROLE OF THE VERTICAL PRESSURE GRADIENT IN WAVE BOUNDARY LAYERS

Karsten Lindegård Jensen[1], B. Mutlu Sumer[1], Giovanna Vittori[2] and Paolo Blondeaux[2]

By direct numerical simulation (DNS) of the flow in an oscillatory boundary layer, it is possible to obtain the pressure field. From the latter, the vertical pressure gradient is determined. Turbulent spots are detected by a criterion involving the vertical pressure gradient. The vertical pressure gradient is also treated as any other turbulence quantity like velocity fluctuations and statistical properties of the vertical pressure gradient are calculated from the DNS data. The presence of a vertical pressure gradient in the near bed region has significant implications for sediment transport.

Keywords: wave boundary layers, turbulence, vertical pressure gradient, DNS, transition to turbulence

INTRODUCTION

Wave boundary layers have been studied extensively over the past three decades or so. These studies cover the entire range of flow regimes, laminar, transitional and turbulent. Observations show that, in the transitional regime, turbulence first emerges in isolated areas where the flow "bursts" with violent oscillations (Carstensen, Sumer and Fredsøe 2010). These areas are called turbulent spots and they grow in time, and once they merge, the flow becomes fully turbulent.

Carstensen et al's. (2010) work was later extended to the case of solitary wave boundary layers (Sumer et al, 2010) and wave boundary layers over a rough bed (Carstensen, Sumer and Fredsøe, 2012)

Mazzuoli, Vittori and Blondeaux (2011) have recently simulated turbulent spots in wave boundary layers by means of Direct Numerical Simulation (DNS) to reproduce the experimental results by Carstensen et al. (2010), and their results have complemented those of Carstensen et al. (2010).

In the present study the same DNS data as in Test 1 of Mazzuoli et al. (2011) are examined in terms of vertical pressure gradient, presumably a new quantity in the analysis of turbulent wave boundary layers.

It turns out that this new approach and the interpretation of the DNS results shed light onto the understanding of laminar-to-turbulent transition in wave boundary layers.

NUMERICAL MODEL

Applying Stokes linear wave theory in shallow waters the orbital motion of the water particles near the seabed becomes parallel to it. In a Cartesian coordinate system, where x_1^* is in the direction of the wave propagation, x_2^* is the vertical and x_3^* points in the spanwise direction (see Fig. 1), the flow in the boundary layer can be studied as an oscillatory flow driven by a pressure gradient determined by

$$\frac{\partial P^*}{\partial x_1^*} = -\rho^* U_{0m}^* \omega^* \sin(\omega^* t^*)\,; \quad \frac{\partial P^*}{\partial x_2^*} = 0; \quad \frac{\partial P^*}{\partial x_3^*} = 0 \tag{1}$$

As in Blondeaux and Vittori (1994), Costamagna et al. (2003) and Mazzuoli et al. (2011), the bottom wall has a small waviness in the x_1^*- and x_3^*-directions, and the vertical coordinate x_2^* is measured from

[1] Technical University of Denmark, Department of Mechanical Engineering, Section for Fluid Mechanics, Coastal and Maritime Engineering, 2800 Kgs. Lyngby, Denmark

[2] University of Genoa, Department of Civil, Chemical and Environmental Engineering, 16146 Genoa, Italy

the mean wall (or bed) level. The waviness of the bottom surface profile η^* is generated by a superimposition of sinusoidal components and is described by

$$x_2^* = \epsilon^* \eta(x_1^*, x_3^*) = \epsilon^* \sum_{n=1}^{N} a_n \cos(\alpha_n^* x_1^* + \gamma_n^* x_3^* + \phi_n) \tag{2}$$

where $\epsilon^* a_n$ is the amplitude of the nth-harmonic component, ϵ^* in the present simulation is taken as $\epsilon^* = 0.005\delta^*$, δ^* being the Stokes length $= \sqrt{2\nu^*/\omega^*}$ and ω^* the angular frequency $= 2\pi/T^*$, T^* the period and ν^* the kinematic viscosity. The waviness is characterized by wave numbers α_n^* and γ_n^* in the x_1^* and x_3^* directions, respectively, ϕ_n is a phase shift and N is the number of terms in the summation. Vittori and Verzicco (1998) investigated the effect of the wall waviness and found that it is necessary to trigger transition to the intermittently turbulent regime, even if the amplitude of the wall waviness is so small that it has no significant influence on turbulence characteristics and the wall can be considered smooth from a macroscopic point of view (Vittori and Verzicco, 1998).

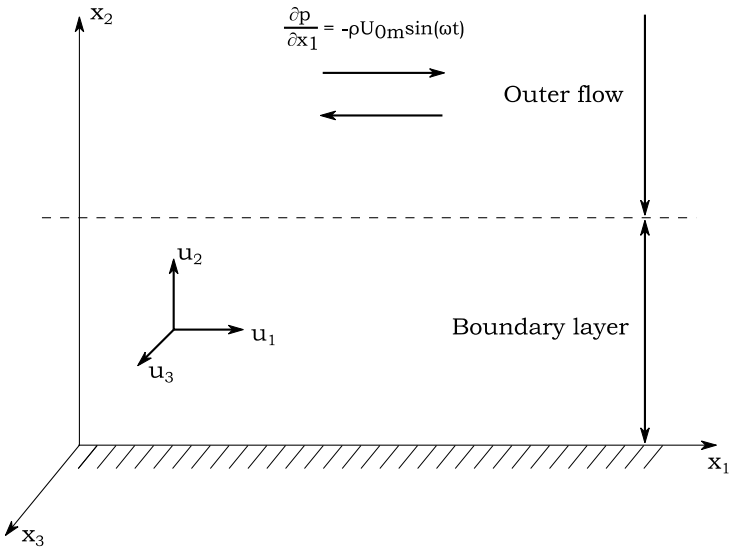

Figure 1. Definition. The outer flow is driven by a pressure gradient in the streamwise direction.

The non-dimensional form of the Navier-Stokes equation reads

$$\frac{\partial u_i}{\partial t} + \frac{R_\delta}{2} u_j \frac{\partial u_i}{\partial x_j} = -\frac{R_\delta}{2} \frac{\partial p}{\partial x_i} - \delta_{i1} \sin(t) + \frac{1}{2} \frac{\partial^2 u_i}{\partial x_k \partial x_k} \qquad for\ i = 1, 2, 3 \tag{3}$$

and continuity equation becomes

$$\frac{\partial u_i}{dx_i} = 0 \qquad for\ i = 1, 2, 3 \tag{4}$$

where the following non-dimensional variables are used

$$t = t^*\omega^*; \quad (x_1, x_2, x_3) = \frac{(x_1^*, x_2^*, x_3^*)}{\delta^*}$$
$$p^* = \frac{p^*}{\rho^* U_{0m}^{*2}}; \quad (u_1, u_2, u_3) = \frac{(u_1^*, u_2^*, u_3^*)}{U_{0m}^*} \tag{5}$$

where t^* is the time, p^* the pressure, u_i^* the velocity in the x_i^* direction, $R_\delta = U_{0m}^*\delta^*/\nu^*$, the Reynolds number, based on the Stokes length δ^*.

Eqs. 4 and 5 are solved numerically in a computational domain the size of which is L_{x1}, L_{x2} and L_{x3} in the streamwise, the vertical and the spanwise directions, respectively (see Table 1). At the bottom wall the no-slip condition is enforced. Since the wall waviness is assumed to be much smaller than the thickness of the laminar boundary layer ($\epsilon = \epsilon^*/\delta^* \ll 1$), the no-slip boundary condition is expanded up to second order in the variable ϵ and is forced at $x_2 = 0$ (Mazzuoli et al., 2011). Since the accuracy of the numerical method employed to solve the Navier Stokes equation is of second order and ϵ is smaller than the size of the first computational grid in the vertical direction, there is consistency between the numerical scheme and boundary condition (Vittori and Verzicco,1998).

At the upper boundary ($x_2 = L_{x2}$), far from the bed, a symmetrical condition is applied. This is the same as requiring the vanishing of the tangential stresses far from the bed. The remaining boundary conditions (x_1x_2 and x_3x_2 planes) are periodic because the turbulent flow is assumed to be homogeneous in the x_3 and x_1 directions.

The mesh is uniform in the x_1 and x_3 directions and non-uniform in the x_2 direction so that the grid points are clustered near the bed (minimum grid size is $0.16\delta^*$ and maximum grid size is $0.59\delta^*$). The method uses second order finite difference approximations for the spatial derivatives and the fraction-step method for the time step in the Navier-Stoke equation. For a more detailed description of the numerical procedure, see Kim and Moin (1985), Orlandi (1989), Vittori and Verzicco (1998) and Costamagna et al. (2003).

Table 1. Numerical parameters for the test. Here $\alpha_n = \alpha_n^*\delta^*$ and $\gamma_n = \gamma_n^*\delta^*$.

test	R_δ	Re	L_{x1}	L_{x2}	L_{x3}	n_1	n_2	n_3	N
1	948	$4.5 \cdot 10^5$	213.6	25.13	75.40	541	65	385	2
test	a_2	a_2	α_1	α_2	γ_1	γ_2	ϕ_1	ϕ_2	-
1	1	0.1	0.5	0	0	1	0	0	-

Test conditions and the properties of the numerical mesh are given in Table 1. In Table 1 $\mathrm{Re} = U_{0m}^* a^*/\nu^*$, where $a^* = U_{0m}^* T^*/(2\pi)$, n_1, n_2 and n_3 are the number of grid points in streamwise, vertical and spanwise direction, respectively. The computational domain should be large enough to contain the largest coherent vortex structure that occurs in the boundary layer simultaneously, the grid size should be small enough to describe the smallest turbulent eddies. To secure this, a fast Fourier transform of the velocity field has been performed and it has been verified that the amplitude of the spectral components with the largest and smallest wave numbers are smaller than a few percent of the maximum amplitude.

Turbulent spots. Laminar-to-turbulent transition

Turbulent spots are isolated areas in an otherwise laminar flow where the flow "bursts" into violent random oscillations, first observed by Carstensen et al. (2010) for wave boundary. These observations were complemented by the DNS simulations of turbulent spots in oscillatory boundary layers by Mazzuoli et al. (2011) and Mazzuoli (2013).

Turbulent spots can be visualized in CFD experiments by various criteria involving "traditional" turbulence quantities such as turbulent kinetic energy production (TKEP ($-\overline{u_i'u_j'}\partial\overline{u_i}/\partial x_j$)), turbulent kinetic energy (TKE ($1/2\overline{u_i'u_i'}$)), wall-shear-stress fluctuations, or velocity fluctuations. Fig. 2a displays the contour plot of the TKEP at a distance $x_2 = 0.24$ from the wall at $\omega t = 45\,°$ (the flow being from left to right) and shows that, turbulent spots can be visualized by the larger values of TKEP. Fig. 2a is accompanied by another contour plot (Fig. 2b), namely the counter plot of the quantity $-\partial p/\partial x_2$, i.e. the pressure gradient in the direction perpendicular to the wall at the same x_2 location and phase as in Fig. 2a:

$$-\frac{\partial p}{dx_2} = -\frac{\partial\left(\frac{p^*}{\rho^* U_{0m}^{*2}}\right)}{\partial\left(\frac{x_2^*}{\delta^*}\right)} \tag{6}$$

Note that the vertical distance $x_2 = 0.24$ (at which these contour plots are given) is the level closest to the wall where the vertical pressure gradient can be resolved in the present DNS simulation. We also note that, for convenience, the minus sign is added to $\partial p/\partial x_2$ so that a positive value of ($-\partial p/\partial x_2$ indicates an upward-directed force on fluid particles. As shown by Fig. 2, the turbulent spots, visualized by the vertical pressure gradient (Fig. 2b), are strikingly similar to those visualized by the TKEP (Fig. 2a).

The DNS simulation indicates that turbulent fluctuations appear at multiple locations in the x_1x_3 plane simultaneously. When they first occur they are rapidly damped. Later, however, around $\omega t = 20°$, they begin to remain sustained, and turbulent spots emerge. Then the spots grow in size until they merge whereby the entire near bed region becomes turbulent at $\omega t = 65°$. These DNS simulations are in qualitative and to some degree quantitative agreement with the works of Jensen et al. (1989) and Carstensen et al. (2010) although the DNS results imply an early transition by O($30 - 40°$). This might be related to (a) the difficult and possible subjective judgments in defining the transition limit experimentally, (b) the higher level of the perturbations in the experimental apparatus.

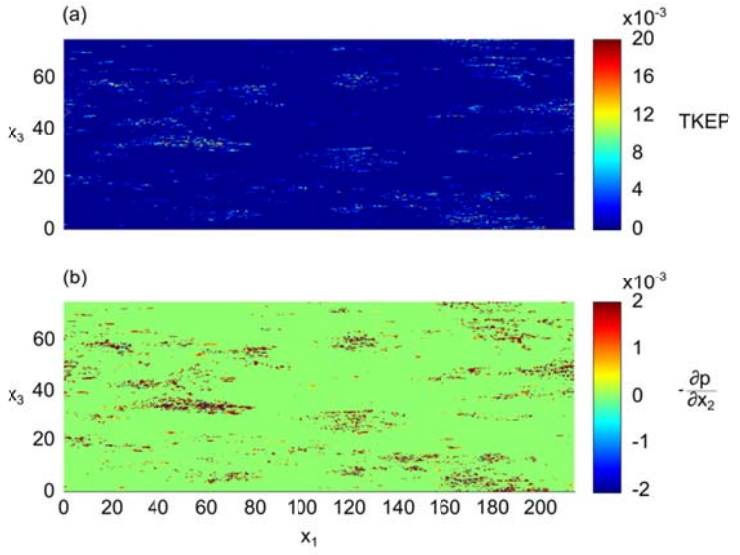

Figure 2.Turbulent spots for ωt = 45˚. The flow is from left to right. Qualitatively the two criteria the vertical pressure gradient and the turbulent kinetic energy production (TKEP) are capable of detecting the same areas where the flow as become turbulent.(a): Turbulent spots using the turbulent kinetic energy production (TKEP) as criterion as Mazzuoli et al. (2011).(b): Using the vertical pressure gradient as criterion.

Statistical analysis of vertical pressure gradient

The analysis of the preceding section has clearly shown that the quantity $(-\partial \mathrm{p}/\partial \mathrm{x}_2)$ can describe the laminar-to-turbulent transition rather well, indeed as good as, for example, the turbulent kinetic energy production. This result stimulated the study highlighted in this section. In this analysis, the vertical pressure gradient, $(-d\mathrm{p}/d\mathrm{x}_2)$, is considered like a turbulence quantity, and the statistical properties of this quantity, namely the mean, and the standard deviation, are calculated from the data obtained in the present DNS simulation. The analysis will be presented in three steps: (1) Bed shear stress; (2) Turbulence quantities; and (3) Vertical pressure gradient. The first two steps are included in the analysis as they prove useful for the analysis of the pressure gradient, the focus of the present study.

Bed shear stress

Fig. 3 displays the time variation of the phase resolved mean bed shear stress, $\overline{\tau_0}$, (averaged over the entire x_1x_3 plane) where $\tau^* = \mu^* \, \partial u_1^*/\partial x_2^*$, and τ_0 is

$$\frac{\tau_0^* \delta^*}{\mu^* U_{0m}^*} = \tau_0 = \frac{\partial u_3}{\partial x_2} \tag{7}$$

As seen from Fig. 3 the bed shear stress leads the free stream by a phase difference of 20˚. This agrees well with the experimental data reported in Jensen et al. (1989) and Carstensen et al. (2010).

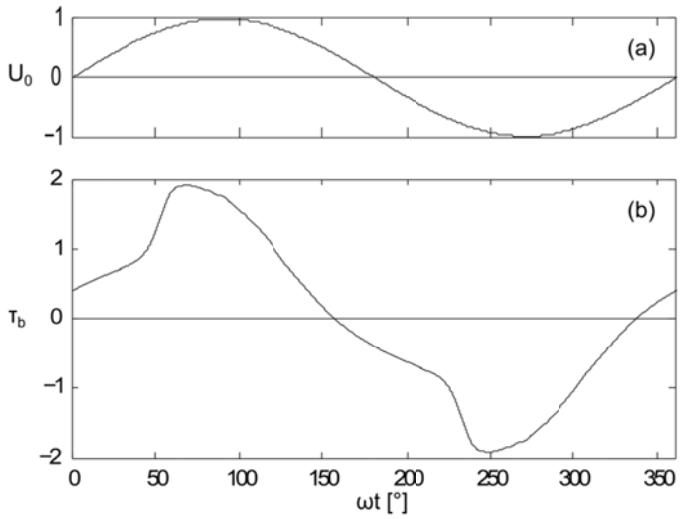

Figure 3. a: The normalized free stream velocity. b: The normalized bed shear in terms of bed friction velocity.

The maximum value of the bed shear stress obtained in the present simulation is $\tau_0 = 1.9$. Using this value and assuming $T = 9.72$s, the wave friction factor defined by

$$f_w = 2\frac{\bar{\tau}^*_{0m}}{\rho^* U^{*2}_{0m}} \tag{8}$$

is found to be $f_w = 0.0040$, and the latter value matches the results from Jensen et al.'s (1989) experiment, $f_w \cong 0.004$

Turbulence quantities

Figs. 4 and 5 present the time evolution of the turbulence quantities in which the turbulence quantities $\left(\overline{u_i'^2}\right)^{1/2}$ $(i = 1, 2, 3)$ and $\overline{u_1' u_2'}$ in which u_i' is the fluctuating component of the velocity u_i. Overbar indicates the special average taken over the entire $x_1 x_3$ plane are plotted versus the distance from the bed, all normalized by the outer flow parameter. This allows for a direct comparison with the results from Spalart and Baldwin (1987) and Jensen et al. (1989). The comparison reveals that the results compares favourably well. The results are however not shown here for reasons of space.

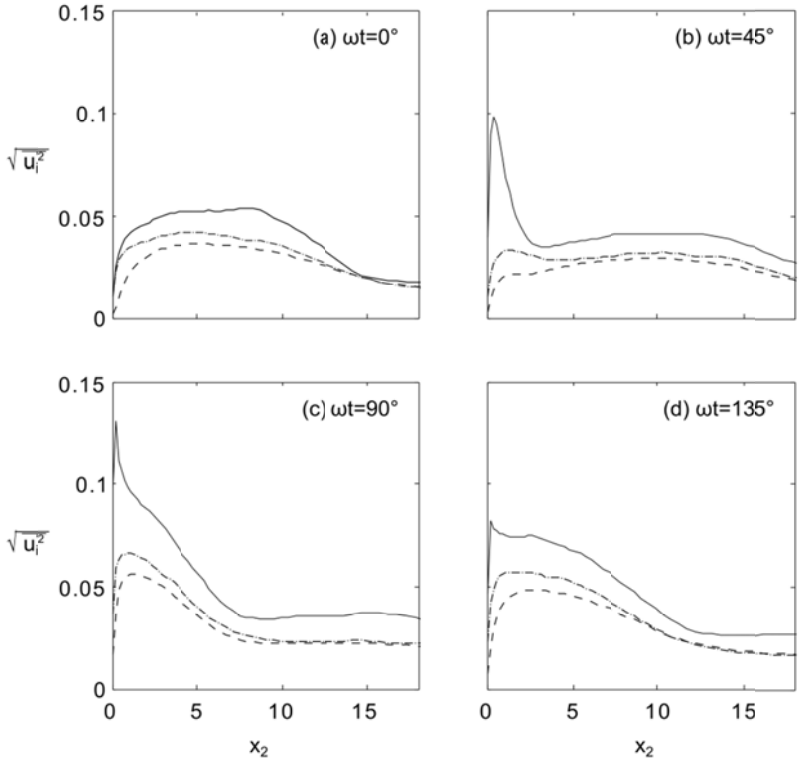

Figure 4. Time evolution of turbulence quantities. R.m.s. values for u_i' for selected phases. ── u_1', – – u_2' and —·— u_3'

The time evolution of the turbulence quantities illustrated in Fig. 4 is given for four selected phase values, $\omega t = 0°, 45°, 90°$ and $135°$. It is seen in Fig. 4a that, with the reversal of the free stream flow ($\omega t = 0°$) turbulence has evidently spread quite a substantial portion of the boundary layer, up to a height of $x_2 = 14$ before it reached its asymptotic value. It is seen that, by the time the phase reaches $\omega t = 45°$ (Panel b), this turbulence is presumably dissipated, and it is only close to the bed that there is a peak in the r.m.s. values of u_1'. As the phase value increases further ($\omega t = 90°$, Panel c) the buildup of turbulence continues in all three velocity components. Finally, with $\omega t = 135°$ (Panel d) the turbulence spreads out as high elevations as $x_2 = 12$. This continuous buildup of turbulence is due to diffusion of turbulence that allows a growing boundary layer over the entire phase until a new boundary layer starts to form at the near bed flow reversal (Jensen et al. 1989).

The same pattern is repeated for the non-dimensional Reynolds stresses illustrated in Fig. 5. In Fig. 5a the Reynolds stresses from the previous period is not yet dissipated. The negative value is because the free stream velocity has just been in the negative direction. In Fig. 5b the turbulence is dissipated and a new buildup has started near the bed. Panels Fig. 5c and Fig. 5d show that the buildup continues until the flow reverses, in exactly the same fashion as in Fig. 4. The results presented in Figs. 4 and 5 are in complete agreement with Jensen et al. (1989). Furthermore, although not shown here for reasons of space, the present results are in accord with the steady boundary layer data for phase values near $\omega t = 90°$, an expected result as the oscillatory boundary layer behaves much the same for these phase values as the streamwise pressure gradient driving the oscillatory boundary layer becomes rather small (and indeed it becomes zero at $\omega t = 90°$) for these phase values.

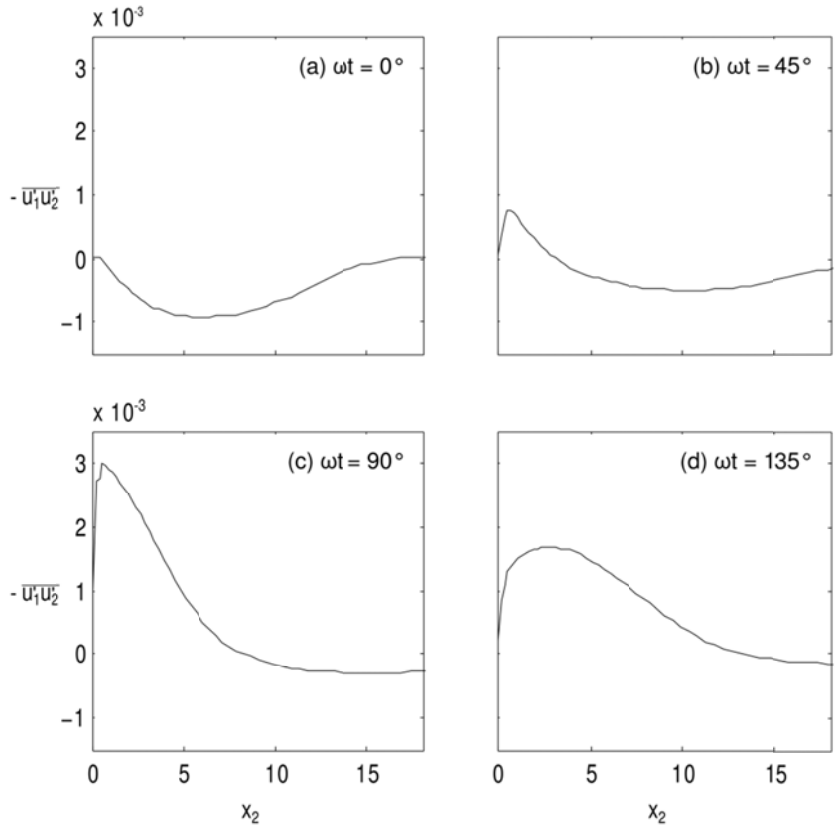

Figure 5. Time evolution of Reynolds stresses $\overline{u_1' u_2'}$ for selected phases.

Vertical pressure gradient

Fig. 6 presents the time evolution of the vertical pressure gradient in non-dimensional form $\overline{\partial p/\partial x_2}$ for the same phase values as in Figs. 4 and 5. Similar to the turbulence quantities in Figs. 4 and 5, the pressure gradient is normalized by the outer flow parameters (Eq. 6), the maximum free stream velocity and the density of the fluid, and plotted versus the non-dimensional distance from the bed x_2, and the averaging (overbar) is taken over the entire plane $x_1 x_3$ plane, as in the case of the turbulence quantities.

Two sets of data are plotted in Fig. 6. The first one (solid lines in the figure) represents the conditional averaged vertical pressure gradient corresponding to $-\partial p/\partial x_2 > 0$ (the upward-directed pressure gradient), while the second set of data (the dashed lines) represents the conditional averaged vertical pressure gradient corresponding to $-\partial p/\partial x_2 < 0$ (the downward-directed pressure gradient).

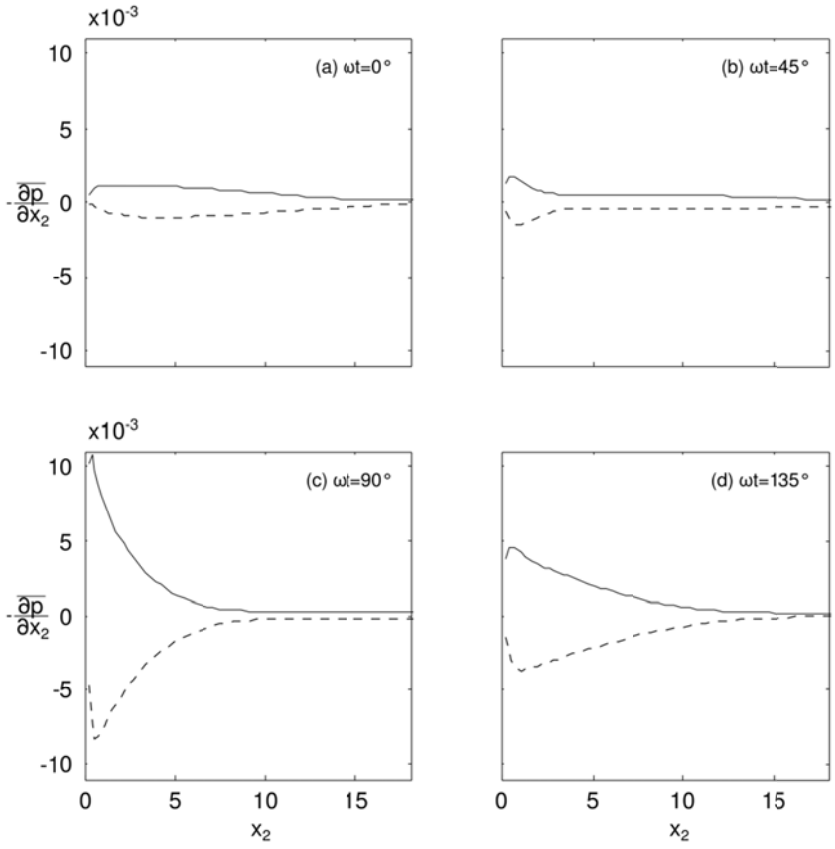

Figure 6. Conditional averaged value of $-\partial p/\partial x_2$ for selected phase values. —— $(-\partial p/\partial x_2 > 0)$ **and — —** $(-\partial p/\partial x_2 < 0)$.

The condition referred to in the preceding paragraph implies that, for upward directed pressure gradient, the fluid particles subject to this pressure gradient will move up, and vice versa. This is clearly for fluid particles with practically zero vertical momentum. For particles with finite vertical momentum, however, the aforementioned vertical pressure gradient will first be used to "consume" the momentum of the fluid particles, before the particles begin to move in the direction dictated by the same vertical pressure gradient.

First of all, Fig. 6 shows that, regardless of the phase value, the vertical pressure gradient $\overline{-\partial \mathrm{p}/\,\partial \mathrm{x}_2}$ appears to be largest very near the bed, in the region associated with the generation of turbulence, $x_2 = \mathrm{O}(1)$. Fig. 6 further shows that $\overline{-\partial \mathrm{p}/\partial \mathrm{x}_2}$ increases tremendously with increasing phase, attaining very large values a $\omega t = 90°$ before it begins to fall off. A third observation from Fig. 6 is that the upward-directed pressure gradient appears to be larger than the downward-directed pressure gradient, and this appears to be the case throughout the phase space. However, what generates the vertical pressure gradient is yet unknown to us. Our efforts will be directed towards this question in our future work.

At this juncture, it is interesting to compare the way in which the vertical pressure gradients evolves (Fig. 6) with that of the turbulence quantities (Figs. 4 and 5). When inspected closely, it will be seen that the turbulence quantities are generated in the region $x_2 = \mathrm{O}(1)$, and the turbulence generated by

the flow is constantly fed into the main body of the flow, revealed by the spreading of the turbulence across the boundary layer up to heights as far as $x_2 = O(15)$. This "diffusion" of turbulence across the boundary layer depth is rather clear even at the phase $\omega t = 0°$ where it is seen that there is a substantial amount of turbulence left from the previous half cycle (Fig. 4, Panel a), as was also revealed by Jensen's work (1989). Now, this feature does not exist in the time evolution of the pressure-gradient process (Fig. 6). This is because the pressure gradient process is not a diffusive process.

The present results reveal that the chain of events occurs in the following manner. First the vertical pressure gradient is generated (practically momentarily) near the bed, and this causes fluid motion in the vertical direction (upwards or downwards depending on the direction of the pressure gradient). This is essentialy the turbulence, and it is known that the turbulent kinetic energy generated this way (represented by $k = 1/2\rho\overline{u_\iota u_\iota}$), a scalar quantity, is governed by a diffusion process, revealed by Fig. 4.

The standard deviation σ for the conditional averaged pressure gradients are seen in Fig. 7 in which σ is defined by

$$\sigma_{\left(-\frac{\partial p}{\partial x_2}\right)} = \overline{\left[\left(-\frac{\partial p}{\partial x_2}\right) - \overline{\left(-\frac{\partial p}{\partial x_2}\right)}\right]^{2}}^{\frac{1}{2}} \tag{9}$$

Averaging (overbar) is, again, over the entire space x_1x_3 plane. In Fig. 7, the solid line represents the condition $-\partial p/\partial x_2 > 0$ and the dashed line $-\partial p/\partial x_2 < 0$. Two things are observed. First the magnitude for the upward directed gradient ($-\partial p/\partial x_2 > 0$) has a larger magnitude than the downward directed pressure gradient ($-\partial p/\partial x_2 < 0$). Secondly the same pattern regarding the development over the phase is repeated for the conditional averaged gradients in Fig. 6. It may also be noted that the standard deviation values can be as much as the mean values (of Figs. 6 and 7).

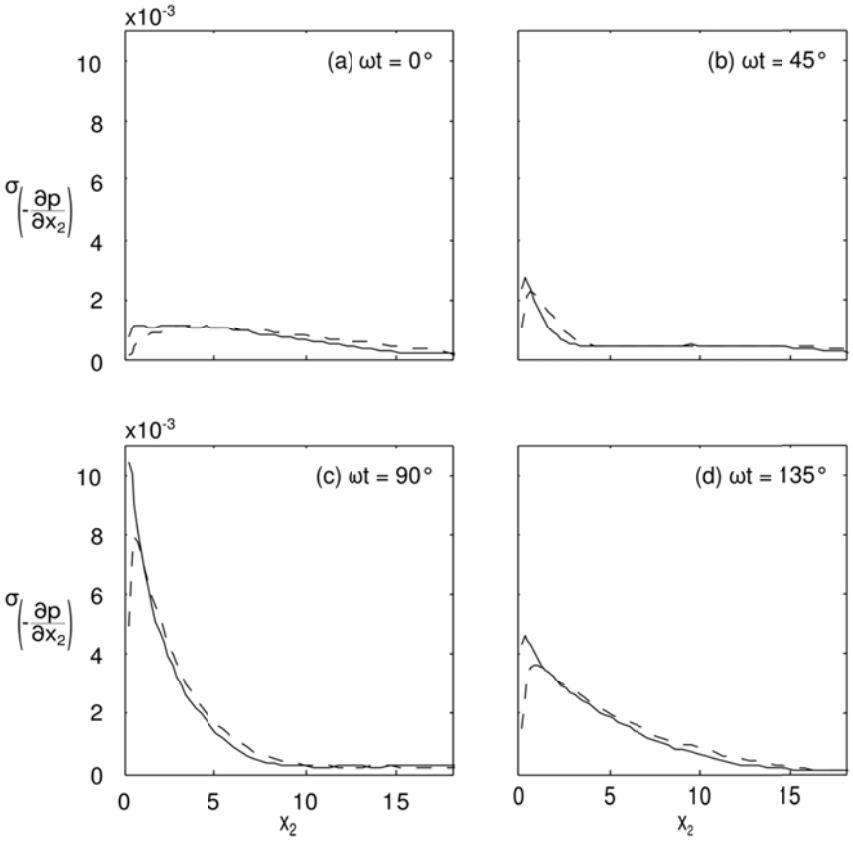

Figure 7. Conditional averaged value of the standard deviation of $-\partial p/\partial x_2$ for selected phase values. —— $\sigma(-\partial p/\partial x_2 > 0)$ and — — $\sigma(-\partial p/\partial x_2 < 0)$.

IMPLICATION FOR SEDIMENT TRANSPORT

The vertical pressure gradient will generate a force on the sediment moving near the bed. The simulation is for a smooth bed, so it's required that the bed behaves as a hydraulic smooth bed. Therefore there is a limitation for the grain size, d^*, that requires the Reynolds grain number to be

$$\frac{d^* U_{fm}^*}{\nu^*} < O(10) \tag{10}$$

The stabilising force on the sediment water mixture in the vertical direction will be the submerged weight W^* (per unit volume) of the mixture where s^* is the specific gravity and n^* the porosity, defined by

$$W^* = (s^* - 1)(1 - n^*) \tag{11}$$

The contribution from the vertical pressure gradient, F^*, to the agitating force on the sediment-water mixtures will be

$$F^* = -\frac{\partial\left(\frac{p^*}{\gamma^*}\right)}{\partial x_2^*} \tag{12}$$

where $\gamma^* = \rho^* g^*$, ρ^* being the density of water and g^* the acceleration due to gravity. If the submerged weight is larger than the agitating forces, $W^* > F^*$, the sediment will not move in the vertical direction. If it is smaller the sediment will move. Considering that other forces like drag and hydrodynamic mass forces will affect the sediment-water-mixture motion we can only look at the contribution from the vertical pressure gradient to the total force needed to move the sediment water mixture and not the total force acting on the sediment-water mixture. Table 2 lists the values for selected typical wave periods and the associated pressure gradient based on the mean values at $\omega t = 90°$ nearest the bed from Fig. 6c and for Eq. 11, $s^* = 2.65$ and $n^* = 0.4$ which are typical values for sediment. The grain sizes in table 2 are selected such that it satisfies Eq. 10.

Table 2. Typical values of wave periods and the magnitude of the vertical pressure gradient at $\omega t = 90°$. Shields parameter, $\theta = U_{fm}^{*2}/(g^*(s^* - 1)d^*)$. Grain Reynolds number is 10 for all cases (See Eq. 10).

T^* [s]	d^* [mm]	$\frac{d^* U_{fm}^*}{\nu^*}$ [−]	θ [−]	F^* [−]	$\frac{F^*}{W^*}$ [−]
5	0.22	10	0.60	0.48	0.48
7.5	0.22	8	0.40	0.26	0.26
10	0.22	7	0.30	0.17	0.17
12.5	0.22	6	0.24	0.12	0.12

As listed in Table 2 the sediment size of 0.22 mm (corresponding to medium sand) fulfils the requirement for the smooth bed. Further Shield's parameter is calculated in order to ensure that the sediment will actually move. As seen all the sediment will move although the largest period is close to incipient motion. The vertical pressure gradient is approximated as an average value over the height of the sediment with the assumption that $x_2 < O(10)$ or in terms of $x_2 = x_2^+/(\overline{\tau_0}\mathrm{R}_\delta)^{1/2} < O(0.25)$. The agitation-force-to-weight ratio F^*/W^* is based on the mean value of $(-\partial p/\partial x_2)$ picked up from Fig. 6. However the instantaneous value of the latter can be as much as two times the mean value, or even larger. Therefore, the F^*/W^* ratio in such cases may even exceed unity, implying that even the pressure gradient alone can suspend the sediment grains from the bed.

CONCLUSIONS

1. Turbulent spots can be detected by a criterion involving the vertical pressure gradient near the bed.
2. The vertical pressure gradient is treated as a turbulence quantity, and classic statistical properties, the mean and the standard deviation, are calculated with conditional averages (depending on whether the gradient is upward or downward directed).
3. Results show that the magnitude of the upward directed conditional averaged pressure gradient is larger than twice the magnitude of the downward directed one.

4. The “life span” of the pressure gradient is seen to be much shorter than that of the velocity fluctuations. This is attributed to the fact that the vertical pressure gradient forces are instantaneous in contrast to the induced velocity fluctuations.

REFERENCES

Blondeaux, P. and G. Vittori. 1994. Wall imperfections as a triggering mechanism for Stokes-layer transition. J. Fluid Mech.264. 107-135.

Carstensen, S., B.M. Sumer, J Fredsøe. 2010. Coherent structures in wave boundary layers. Part 1, J. Fluid Mech. 646. 169-206.

Carstensen, S., B. M. Sumer and J. Fredsøe. 2012. A note on turbulent spots over rough bed in turbulent boundary layers. Physics of Fluids. 24.

Costamagna, P., G. Vittori and P. Blondeaux. 2003. Coherent structures in oscillatory boundary layers. J. Fluid Mech. 474. 1-33.

Jensen, B.L., B.M. Sumer and J. Fredsøe. 1989. Turbulent oscillatory boundary layers at high Reynolds numbers. J. Fluid Mech. 206. 265-297.

Kim, J. and P. Moin. 1985. Application of a fractional step method to incompressible Navier-Stokes equations. Journal of computational physics. 59. 308-323.

Mazzuoli, M., G. Vittori and P. Blondeaux. 2011. Turbulent spots in oscillatory boundary layers. J. Fluid Mech. 685. 365-376.

Mazzuoli, M., 2013. Transition to turbulence in an oscillatory boundary layer and its effects on the motion of a rigid particle. Ph.D. Thesis. University of Genoa. Department of Civil, Chemical and Environmental Engineering.

Orlandi, P. 1989. A numerical method for direct simulation of turbulence in complex geometries. Annual Research Brief. 215. Center for Turbulence Research, Standford University.

Spalart P. R. and B. S. Baldwin. Direct simulation of a turbulent oscillating boundary layer. NASA Technical Memorandum 89460. Ames Research Center. Moffett Field, California.

Sumer B. M., P. Jensen, L. B. Sørensen, J. Fredsøe, P. F. L. Lui and S. Carstensen. Coherent structures in wave boundary layers. Part 2. Solitary motion. J. Fluid Mech. 646. 207-231.

Vittori, G. and R. Verzicco. 1998. Direct numerical simulation of transition in an oscillatory boundary layer. J. Fluid Mech. 371. 207-232.